Astronomy
&
Astrophysics

Extreme coronagraphy with an adaptive hologram

Simulations of exo-planet imaging

D. Ricci[1,*], H. Le Coroller[2], and A. Labeyrie[3]

[1] Département d'Astrophysique, Géophysique et Océanographie, Bât. B5C, Sart Tilman, Université de Liège, 4000 Liege 1, Belgium
    e-mail: ricci@astro.ulg.ac.be
[2] Observatoire de Haute Provence, 04870 Saint Michel l'Observatoire, France
    e-mail: herve.lecoroller@oamp.fr
[3] Collège de France, 11, place Marcelin Berthelot, 75231 Paris Cedex 05, France
    e-mail: antoine.labeyrie@obs-azur.fr

ABSTRACT

Aims. We present a solution to improve the performance of coronagraphs for the detection of exo-planets.
Methods. We simulate numerically several kinds of coronagraphic systems, with the aim of evaluating the gain obtained with an adaptive hologram.
Results. The detection limit in flux ratio between a star and a planet (F_s/F_p) observed with an apodized Lyot coronagraph characterized by wavefront bumpiness imperfections of $\lambda/20$ (resp. $\lambda/100$) turns out to be increased by a factor of $10^{3.4}$ (resp. $10^{5.1}$) when equipped with a hologram.
Conclusions. This technique could provide direct imaging of an exo-Earth at a distance of 11 parsec with a 6.5 m space telescope such as the JWST with the optical quality of the HST.

Key words. instrumentation: detectors – instrumentation: miscellaneous – stars: planetary systems – instrumentation: interferometers

1. Introduction

Most of the 300 or so exo-planets discovered since 1995 (Mayor et al. 1995) have been detected by the radial velocity or the photometric transit methods. In a few cases, transits could be observed spectroscopically and provided data on chemical composition and temperature (Swain et al. 2009). A few sufficiently bright planets were imaged from the ground, with adaptive optics in the near-infrared, first by Chauvin et al. (2004), and more recently by Marois et al. (2008), who removed most of the unwanted diffracted starlight by "angular differential imaging". Another such detection (Kalas et al. 2008) was made, in yellow and red light, with the Hubble Space Telescope. The direct imaging of weaker extra-solar planets, including exo-Earths about 10^{10} times fainter than their parent star at visible wavelengths, remains an enormous challenge since the residual starlight in the image must be removed very efficiently to allow the detection of faint planet images.

The coronagraphic techniques developed since the solar coronagraph of Lyot (1939), particularly in recent years, have significantly improved its nulling gain, which was limited to about 10 000. The "Lyot coronagraph" was improved by replacing the opaque mask with phase masks (Roddier & Roddier 1997; Riaud et al. 2001), which attenuated the background level below 10^{-7} (Riaud et al. 2003). The stronger chromatic dependance of phase masks could be mitigated with devices such as the achromatic annular groove phase mask (Mawet et al. 2007).

One can also improve the existing coronagraphs and erase the rings of the stellar point-spread function (PSF) by apodizing the pupil, for example using prolate functions

(Aime et al. 2002; Soummer et al. 2003). Unfortunately, a large fraction of the light is absorbed by the apodization mask. The loss is avoided with an apodizing device (Guyon 2003; Guyon et al. 2007) using a pair of distorted mirrors to modify the light distribution across the pupil. With this loss-less achromatic apodization, exo-planets as faint as 10^{-10} can in principle be directly imaged.

However, in practice, even a theoretically perfect coronagraph is greatly affected by the residual bumpiness of the incoming stellar wavefront, caused by imperfect mirror polishing or residual atmospheric turbulence, which cannot be perfectly corrected by adaptive optics. The residual halo of starlight in the image typically exhibits a speckle pattern at a relative level much higher than 10^{-10}. Maréchal's formula (Labeyrie et al. 2006) shows that to detect an exo-planet 10^9 times weaker than its parent star with a 10 m mirror operating at 1 μm, the RMS wavefront error among 10 cm patches, such as obtained by 10 000 actuators, should remain below 0.5 nm.

Since such accuracy is not achievable with the present figuring techniques, one method to remove the residues is to add stages of adaptive elements. Several adaptive devices proposed in the literature (Codona & Angel 2004; Labeyrie 2004; Putnam et al. 2006) use the following interesting property: if the star is unresolved, the light of the speckle halo is coherent with that of the central source, usually absorbed by the Lyot mask. This light in principle can be made to interfere destructively with the speckle halo. It improves the detectability of the faint non-coherent exo-planet, thus relaxing the accuracy of the AO actuators.

Here, we present simulations with the adaptive hologram method proposed by Labeyrie (2004). Located close to the Lyot
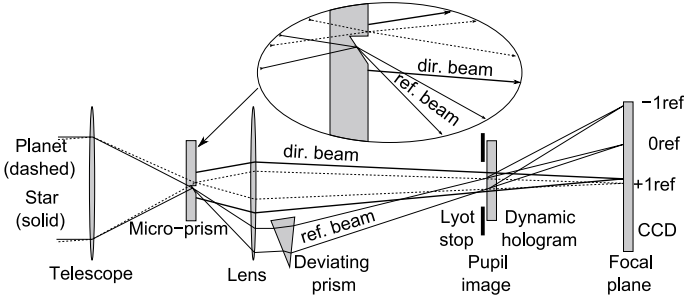

Fig. 1. Holographic coronagraph using a modified Lyot train. The focal occulter is replaced by a deviating micro-prism which separates the star's geometric beam for use as the holographic reference beam, while preserving the outer diffracted rings and speckles, together with the images of planets, forming the direct beam. The micro-prism size, amounting in our simulations to $(8\lambda f/D)$ or 13.5 μm in visible light at $F/3$, can vary between that of the Airy peak and a dozen rings. Equivalently, the micro-prism can also be replaced by a reflective focal plane with a hole selecting the reference beam. A larger deviating prism deflects the reference beam in such a way that it intersects the direct beam in the relayed pupil image where the Lyot stop is located. A dynamic hologram, located at the same position, first records the interference fringes produced by both intersecting beams, and then reconstructs a copy of the star's direct wavefront, without the planet's contribution. The hologram is made to introduce a π phase shift in the reconstructed beam, causing it to interfere destructively with the "live" stellar wavefront (direct beam) also transmitted through it by zero-order diffraction, thus nulling the star's speckles and improving the planet's contrast in the relayed sky image detected by a CCD camera. The lens relays the telescope aperture at the pupil plane and its focal plane at the camera. In the final image, the reference beam is diffracted by the hologram into several orders (−1ref, 0ref, and +1ref in the figure). The order "+1ref" is a reconstruction of the speckled wavefront, phase-shifted by π.
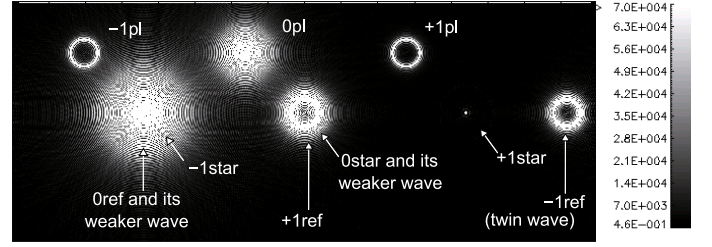

Fig. 2. Simulation of an imaged star-planet system in a Lyot coronagraph equipped with an adaptive hologram (see Fig. 1). Here, for clarity, the planet is particularly bright and far from the parent star. The diffracted orders −1, 0 and +1 of the planet are noted respectively −1pl, 0pl and +1pl. The orders −1, 0 and +1 of the star are noted respectively −1star, 0star and +1star. The order +1star looks faint in this figure because it is fainter than the direct flux of the star (0star) and the reference beam (0ref). The orders −1 (twin wave), 0 and +1 of the reference beam are noted respectively −1ref, 0ref and +1ref. Star nulling is caused by the destructive interference of its order 0 (0star) and the order +1 of the reference beam (+1ref), both superposed on the detector. Here, no π phase shift is introduced in the reference beam, so as to show the diffracted orders +1ref, and 0star. The "twin wave" falls out of the detector at left, but here spuriously appears at right due to aliasing, itself caused by the moderate sampling which we had to use in the hologram.

stop, a hologram removes most of the residual star light by adding to it a phase-shifted copy of its wavefront. In Sect. 2 we describe the optical design of the holographic technique adapted to the traditional Lyot coronagraphs. In Sect. 3 we discuss the adaptive hologram technology. In Sect. 4 we give an analytic description of the diffracted orders generated by the hologram and discuss how to optimize the parameters of the system. In Sect. 5 we show the results of our numerical simulations, discussing the gain obtained under different conditions: ideal ones (Sect. 5.1) and with static wavefront bumpiness and photon noise (Sects. 5.2, 5.3). Finally, Sect. 6 deals with the degrading effect of a star which is partially resolved, its possible mitigation, and the design of an achromatized version.

2. Coronagraph design improved with an adaptive hologram

As previously described (Labeyrie & Le Coroller 2004; Labeyrie 2004), and shown in Fig. 1, the focal occulter in a Lyot coronagraph can be built in the form of a micro-prism deflector preserving most star-light to produce an off-set reference wave. It interferes with the direct wave in order to generate a hologram which is initially recorded in the pupil plane near the Lyot stop, and then exploited for nulling most starlight while preserving the planet's image formation. Depending on the focal ratios, the reference beam may intersect the direct beam at an angle of several degrees. We note ψ_d and $I_d = |\psi_d|^2$ the complex amplitude of the direct beam and its intensity at a point P of the hologram's plane (see Fig. 1), while ψ_r and $I_r = |\psi_r|^2$ are the corresponding values for the reference beam.

The interference between the reference beam and the direct beam creates fringes in the speckles of the hologram (see Figs. 3 and 4). The fringes of the recorded hologram behave like a grating, diffracting several orders which become focused in the focal plane (see Fig. 2). We give a more complete and detailed analysis of the creation and role of the diffraction orders below. The complex amplitude resulting from the interference of the two beams at point P in the pupil is

$$\psi = \psi_d + \psi_r, \tag{1}$$

while the intensity I is

$$\begin{aligned} I &= \psi\psi^* \\ &= (\psi_d + \psi_r)(\psi_d^* + \psi_r^*) \\ &= I_r + \psi_d\psi_r^* + \psi_d^*\psi_r + I_d \\ &= I_r \left[1 + \frac{\psi_r^*\psi_d}{I_r} + \frac{\psi_r\psi_d^*}{I_r} + \frac{I_d}{I_r} \right]. \end{aligned} \tag{2}$$

The hologram has an amplitude transmittance $\tau = I^{\gamma/2}$ where γ is the classical intensity contrast in photographic materials (Perez 2000). By illuminating the recorded hologram with the reference beam only, a reconstructed image of the star's speckles appears on the detector, noted +1ref in Fig. 2. Using a reference beam phase-shifted by π, we obtain the same image phase-shifted by π if the hologram is a positive print. Note that in the article of Labeyrie & Le Coroller (2004) the π shift was obtained with a negative hologram, which is equivalent. Finally, the order 0 of the direct beam (0star) adds destructively with the order "+1ref", thus nulling the residual speckles of the star.

The planet's light, being incoherent with the reference beam and little affected by the micro-prism, is not reconstructed by the hologram, and therefore escapes nulling. If we illuminate the recorded hologram with the reference beam, now phase-shifted by π, the transmitted complex amplitude becomes:

$$\psi = \tau\left(\psi_d + \psi_r e^{i\pi}\right) = \tau\left(\psi_d - \psi_r\right). \tag{3}$$

If $\gamma = 2$, the usual value considered optimal in holographic practice, the product of both factors having respectively four and two
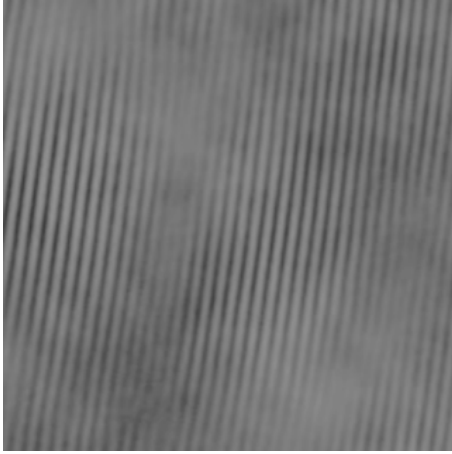
Fig. 3. Small part of a hologram obtained with a laboratory simulator designed according to Fig. 1, suitably magnified to display the low-contrast fringes within the speckles.

terms gives eight terms. As expected, since the reconstructed direct wave is π-shifted with respect to the transmitted direct wave, the corresponding pair of terms cancels. Another pair of terms also cancels for a related reason. The expression thus simplified is:

$$\psi = -I_r\psi_r + I_d\psi_d - \psi_r^2\psi_d^* + \psi_r^*\psi_d^2. \tag{4}$$

The remaining terms of Eq. (4) represent various orders diffracted by the hologram, locally behaving like a diffraction grating, and becoming separated on the camera. Some of them widely spread their speckled light on the camera (see Fig. 2), thereby degrading the visibility of planet peaks, which are imaged through the hologram without being much affected by it. It is of interest to discuss the impact of each term on the planet detection:

1. the term $I_r\psi_r$ is the transmitted reference wave, producing an intense but sharp focus on the camera (order 0 of the reference beam; 0ref in Fig. 2). Apodizing the reference beam improves the nulling depth since its Airy rings in its zero-order image pattern become attenuated, and thus contaminate less the planet's image. Such apodization occurs naturally if the micro-prism separator selects the central Airy peak down to its first dark ring. Additional spatial filtering can be achieved at the micro-prism if needed;
2. the term $I_d\psi_d$ describes a wave that propagates close to the direct stellar residue wave ($I_r\psi_d$), nulled by the hologram, but with attenuated and spatially modulated intensity. This term is called the "weaker wave" in Fig. 2. The modulation causes some diffractive spreading on the camera, contaminating the planet image. This is mitigated by using a very intense reference beam, relative to the direct beam, so that $I_d\psi_d \ll I_r\psi_d$. The intensity thus achievable, as limited by the energy content of the Airy peak in the telescope's focal plane, defines the maximal possible gain with a hologram. This suggests that the maximum nulling achievable is:

$$G \approx \frac{\sum_p I_r^2}{\sum_p I_d^2}, \tag{5}$$

where the $\sum_p$ summing extends to all points of the pupil plane that are not blocked by the Lyot stop. The numerical simulations support this estimate;
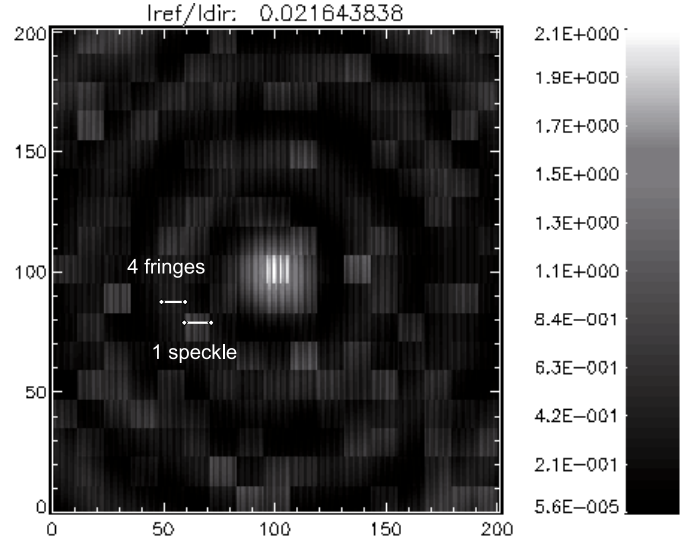

Fig. 4. Numerical simulation of the central part of a hologram recorded in the pupil with reference beam at 65° incidence. For a contrasted display here, the wave bumpiness is adjusted at the $\lambda/40$ level, at $\lambda = 550$ nm, and the reference beam intensity is much reduced, to show both the speckles and the finer fringes within them. There are approximately four fringes per speckle, and four pixels per fringe period. The total pixel count is 1599×1599, only 200×200 of which are displayed here.

3. the term $\psi_r^*\psi_d^2$ is the order $+1$ of the direct beam ($+1$star in Fig. 2);
4. $\psi_r^2\psi_d^*$ is a wave similar to the direct beam (direct stellar residue wave), since its complex amplitude is proportional to the conjugate of ψ_d. This last wave is termed the "twin wave" (order -1 of the reference beam; -1ref in Fig. 2). Its contamination is discussed in Sect. 4.

The order -1 of the direct beam (-1star) cancels with the wave $I_d\psi_r$ that propagates close to the order 0 of the reference beam.

3. Adaptive hologram technology

A dynamic, or adaptive, hologram works both as a wavefront sensor and an actuator array, thus behaving like the feedback loop of conventional adaptive optics. In the absence of rewritable holographic materials having enough light sensitivity and response speed, the hologram's sensing and playing functions can also be achieved by two separate components: a camera and a Spatial Light Modulator (SLM). To detect and process the light beam simultaneously, the camera can be fed by a beam splitter while the SLM is located in the relayed pupil, i.e. at the hologram position indicated in Fig. 1. The latter can be driven by a video signal from the former, at the image rates of standard television, in the absence faster versions. Both components are small and commercially available devices which can fit, together with the beam-splitter, within a cubic inch. Of interest are EM-CCD camera chips, incorporating electron multiplication which makes them nearly photon-limited at low light levels; and SLMs such as those using a liquid crystal film on a silicon matrix, currently available with 1280×720 pixels (see www.cambridgecorrelators.com/products.html). Such existing components are readily usable to test a holographic coronagraph on a laboratory bench and then on a telescope, particularly at red and near infra-red wavelengths where the lifetime of speckles is longer. Inserting a computer or dedicated fast processor in the video connection is useful to adjust the π phase shift,

the gamma contrast, etc. of the printed hologram. Much slower speeds suffice in space, where an artificial star such as a remote laser source can in principle be used to record the hologram.

With these existing components, a typical observing sequence involves the near simultaneous printing of the hologram with the live recorded pattern.

4. Numerical simulations with optimized hologram parameters

We adjusted the size of the micro-prism to that of the fourth dark ring in the Airy pattern; the planet was placed in the fifth ring. This reproduces the angular separation between a star and an Earth-like planet located at 1 UA from its parent star, at 11 pc from us (like the Sun and Earth as seen from Gliese 436), and observed with a 6.5 m telescope. In order to simplify the computations, we coarsely simulated the mirror bumpiness or turbulence with a square grid of bumps with random amplitudes, and verified that the shape of the phase cells on the mirror do not affect our results.

For minimal calculation noise, which represents possible problem given the high dynamic range considered, while keeping a reasonable computation time and usage of our 2GB RAM memory, we used 1599×1599 pixel arrays, with a pupil spanning 402 sampling points.

The bumpiness of the incoming wavefront is converted into intensity speckles having random phases in the relayed pupil, i.e. in the hologram, in response to the occultation of the Airy peak in the focal plane. In the pupil plane, the interference with the oblique reference beam generates the finer fringes seen within each speckle (Figs. 3 and 4). For a good sampling in the hologram, four pixels at least are needed per fringe period, and simultaneously at least four fringes per speckle. Increasing the angle θ between the direct and reference beams increases the number of fringes per speckle, but decreases the number of pixels per fringe. It also increases the spacing of the diffracted orders in the focal plane, which improves the contrast of the planet's peak. In our simulation, we used about 4 pixels per fringe for an angle $\theta = 65°$ (see Fig. 4). This corresponds to at least 4 fringes per speckle, if the typical scale of the bumpiness at the entrance pupil is larger than 12×12 pixels. For optimal performance, it is important to adjust the following parameters:

- In accordance with the classical theory of holograms, the reference beam must be substantially more intense for a faithful wavefront reconstruction by the hologram, as apparent in the second term of Eq. (4). In practice here, the hologram's nulling gain is proportional to the square intensity ratio, i.e. $\approx 10^3$ in our numerical simulation with wavefront bumpiness imperfections at $\lambda/20$ at $\lambda = 550$ nm. This ratio is limited in practice by the energy content of the Airy peak, diverted by the micro-prism to form the reference beam. The size of the micro-prism or attached filtering aperture, possibly apodized, should be optimized for maximal light collection while keeping a flat wave front. We found that an aperture sized like the Airy peak is optimal in this respect and also to minimize the inner working angle.
- As in conventional Lyot coronagraphs, the size of the Lyot stop was adjusted to block the bright edge of the pupil image.
- Based upon Eq. (4), we conclude that an optimal value for γ is 2 using a positive print, with a phase shifter then introduced in the reference beam during read-out, and -2 if it is negative.

Table 1. Summary of the approximate limiting detection of the flux ratio F_s/F_p with the different configurations mentioned in Sect. 5 without photon noise[1].

Conditions	(A)	(B)	(C)	(D)
Perfect conditions	$10^{3.2}$	$10^{11.0}$	$10^{11.0}$	$10^{11.0}$
$\lambda/100$	$10^{3.5}$	$10^{5.7}$	$10^{7.6}$	$10^{10.8}$
$\lambda/20$	$10^{3.5}$	$10^{4.5}$	$10^{6.2}$	$10^{7.9}$

[1] "$\lambda/100$" and "$\lambda/20$" are referred to the gain after the introduction of wavefront bumpiness imperfection at $\lambda/100$ and $\lambda/20$ (Sect. 5.2).

- The twin wave is described by the term $\psi_r^2 \psi_d^*$ in Eq. (4). It gives a focal image identical to the direct wave, but shifted, and non-overlapping if the reference beam angle, with respect to the direct beam, exceeds the apparent pupil size. In our simulations, however, the pixel sampling of the hologram was insufficient to properly generate the twin wave, causing it to be aliased by the Fourier transform algorithm, and to appear in the final image at an incorrect "folded" location which contaminated the planet image (See Fig. 2). The aliasing effect causes the twin wave to be nearer to the 0 order of the direct beam (and then to disturb the flux of the planet) than if it was not aliased.

In order to remove such numerical effects, we simulated a suppressed twin wave by removing the corresponding term, in complex amplitude, in the numerical calculation, and found an improved detection sensitivity, part of which may result from the removed aliasing effect.

In this paper, we did not study the physical effect of the twin wave, but we know that the solution is intermediate between the case including the twin wave (C in Table 1) and the case where its effect is analytically subtracted (D in Table 1). More realistic simulations of the twin wave's effect are desirable in further work, and this may require non-FFT calculation methods (Soummer et al. 2007).

Nevertheless, twin waves can be eliminated by using a thick hologram, also known as a Lippmann-Bragg hologram, in order to work in the case (D) of Table 1. These have stratified nodal planes, rather than fringes, which selectively reflect a single first-order wave. Then, the hologram works like a "blazed grating", sending most light in the reconstructed image (order +1ref).

5. Gain evaluation

Using the optimizations listed in Sect. 4, we were able to reproduce a wide range of coronagraph configurations, in order to compare their planet detection limit versus the "star/planet" flux ratio (F_s/F_p).

(A) Classical Lyot coronagraph;
(B) Apodized Lyot coronagraph;
(C) Apodized Lyot coronagraph with hologram and an apodized reference beam;
(D) Apodized Lyot coronagraph with hologram, apodized reference beam, and subtracted twin wave.

The performance is evaluated under three different conditions: ideal ones (no mirror imperfections and absence of photon noise); with the introduction of mirror imperfections and finally with photon noise in addition to the mirror imperfection. These steps are treated in the following subsections, and summarized
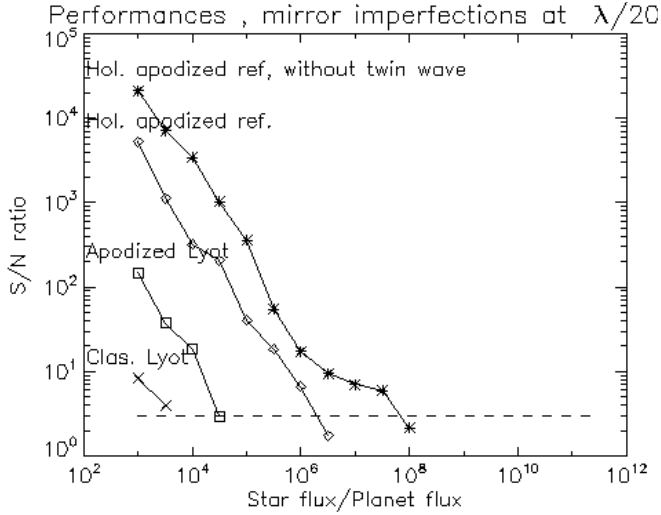
Fig. 5. Approximate S/N ratio of planet detection vs. the star/planet flux ratio, in the presence of $\lambda/20$ wavefront bumpiness at $\lambda = 550$ nm and without photon noise (see Sect. 5.2). The detection limit (dashed) was chosen at $S/N = 3$. We find a value of $\sum I_r^2 / \sum I_d^2 \approx 10^3$ for the solutions providing the hologram.
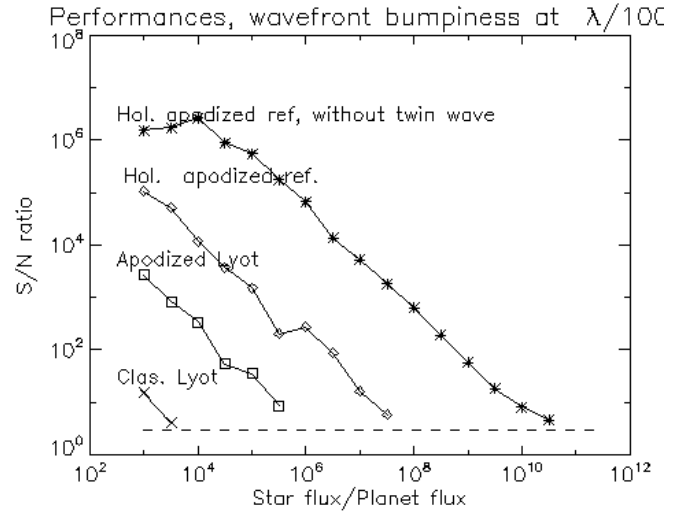
in Table 1 for the two first conditions. The speckle noise was coarsely evaluated in the images using the following equation:

$$\frac{\bar{I}_{\text{peak}} - \bar{I}_{\text{speckle}}}{\sigma_{\text{speckle}}} \tag{6}$$

where $\bar{I}_{\text{peak}}$ is the mean intensity at the position of the planet; $\bar{I}_{\text{speckle}}$ is the mean intensity of the speckles near the planet position, and σ_{speckle} is the corresponding root mean square fluctuation.

5.1. Gain with a perfect mirror

The first results are obtained under the assumption of perfect conditions, in the absence of mirror bumpiness and photon noise.

For the classical Lyot coronagraph (A), we obtain a detection limit in flux ratio of $F_s/F_p = 10^{3.2}$. In the case of the apodized Lyot coronagraph (B), the detection limit is increased to $10^{11.0}$. Introducing the hologram in the optical scheme with the apodization of the reference beam (C), the limit is $10^{11.0}$. Our simulations appear to be limited to this range by numerical noise. The hologram becomes most valuable in the presence of mirror imperfections.

5.2. Gain with bumpy mirror

In order to test the performance under more realistic conditions, we have introduced a random static bumpiness on the incoming wavefront, with a $\lambda/20$ peak-to-valley amplitude. We also performed simulations at $\lambda/100$, a situation intermediate between perfect conditions and $\lambda/20$ amplitude. The results are shown in Figs. 5 to 7.

The detection limit in flux ratio with a $\lambda/20$ wavefront bumpiness is $F_s/F_p = 10^{3.5}$ with the classical Lyot coronagraph (A); $10^{4.5}$ with the apodized Lyot coronagraph (B); $10^{6.2}$ with the hologram and apodized reference beam (C); and $10^{7.9}$ after subtracting the twin wave (D). At $\lambda/100$ we find $F_s/F_p = 10^{3.5}$ with the classical Lyot (A); $10^{5.7}$ with the apodized
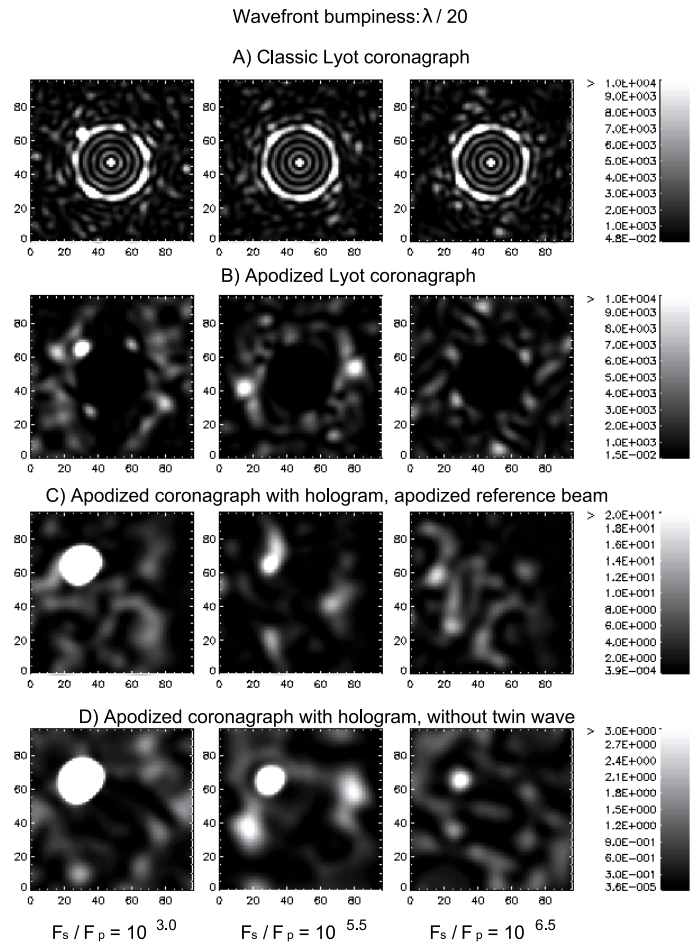

Fig. 6. Approximate S/N ratio of planet detection vs. the star/planet flux ratio, in the presence of $\lambda/100$ wavefront bumpiness, at $\lambda = 550$ nm and without photon noise (see Sect. 5.2). The detection limit (dashed) was chosen at $S/N = 3$. We find a value of $\sum I_r^2 / \sum I_d^2 \approx 10^6$ for the solutions providing the hologram.

Fig. 7. The four rows show simulated images with the A, B, C and D coronagraph types mentioned in Sect. 5. The star/planet flux ratio is $10^{3.0}$ in the left column, $10^{5.5}$ in the central column, and $10^{6.5}$ in the right column. The wavefront bumpiness is $\lambda/20$ as described in Sect. 5.2. The intensity scales at right indicate the number of photons per pixel, for a star with magnitude $m_V = 7$, a telescope diameter $D = 6.5$ m, $\lambda = 550$ nm and spectral bandwidth $\Delta\lambda = 10$ nm. The exposure time is 60 s for both the hologram and the science camera.
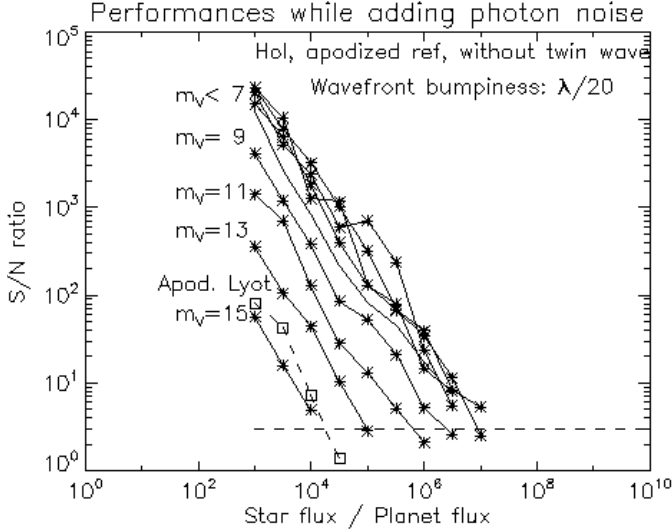
Fig. 8. Approximate S/N ratio as a function of the star/planet flux ratio, evaluated with $\lambda/20$ wavefront bumpiness and photon noise (see Sect. 5.3) for the coronagraph (D). curves are calculated for different stellar magnitudes, assuming $D = 6.5$ m, 60 s exposures, $\lambda = 550$ nm and $\Delta\lambda = 10$ nm. The performances of the apodized Lyot coronagraph at $m_V = 7$ are also plotted (squares). The detection limit (dashed line) was chosen at $S/N = 3$.
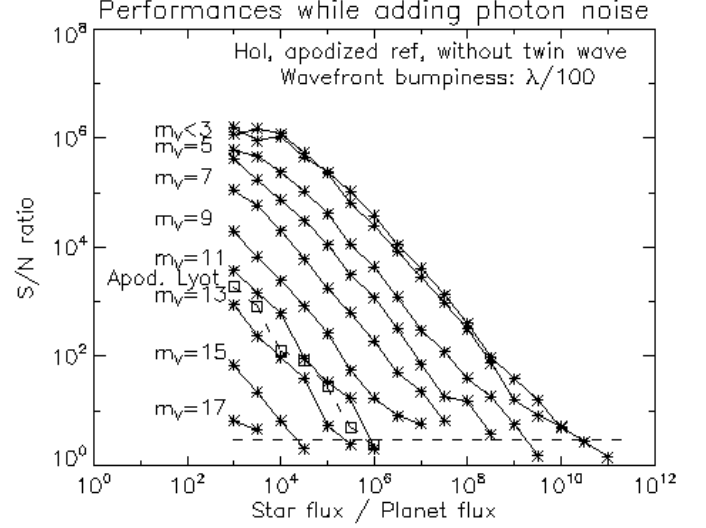
Fig. 9. Approximate S/N ratio as a function of the star/planet flux ratio, evaluated with $\lambda/100$ wavefront bumpiness and photon noise (see Sect. 5.3) for the coronagraph (D). curves are calculated for different stellar magnitudes, assuming $D = 6.5$ m, 60 s exposures, $\lambda = 550$ nm and $\Delta\lambda = 10$ nm. The performances of the apodized Lyot coronagraph at $m_V = 7$ are also plotted (squares). The detection limit (dashed line) was chosen at $S/N = 3$.

solution (B); $10^{7.6}$ with the hologram and apodized reference beam (C); and $10^{10.8}$ after subtracting the twin wave (D).

The results with mirror bumpiness reveal the large gain then obtained with the introduction of the hologram, especially when subtracting the twin wave. Indeed, with $\lambda/20$ wavefront bumpiness, it is not possible to detect a planet with an apodized Lyot coronagraph if the ratio F_s/F_p is larger than $10^{4.5}$ (see Fig. 7). This limit is pushed to $10^{7.9}$ using the same coronagraph equipped with a hologram and after the subtraction of the twin wave. The detection limit is increased by a factor $10^{3.4}$. This number is about equal to the intensity ratio, predicted by the analytical estimation (see Eq. (5)).

5.3. Gain with bumpy mirror and photon noise

After having tested the coronagraphs under perfect conditions and in the presence of mirror bumpiness, we added photon noise. Unless the hologram is recorded with infinitely many photons, its recorded fringes are noisy, and this degrades the nulling depth in the camera image by creating a broad speckled halo, which degrades the visibility of the planet's peak. It can be shown that the sensitivity limitation, regarding the detection of faint planets, is then ultimately the same as with a conventional adaptive system feeding a perfect coronagraph or apodizer, where the nulling depth is similarly limited by the number of photons detected by the wave sensor. The calculation given in the former case (Labeyrie 2004) indeed also applies to the latter: N_p photons detected by either a hologram or a conventional wave sensor limit the achievable peak/halo nulling depth G to $G_{max} = N_p$. In both cases, as well as with a Mach-Zehnder interference nuller (Codona & Angel 2004; Putnam et al. 2006), it follows that recording and observing exposures lasting the same time leave at least one star photon per speckle in the nulled camera image, which can be low enough to detect planet peaks containing several photons. The holographic nuller has no theoretical advantage in this respect.

Hybrid forms using both conventional adaptive optics for coarse wavefront correction, and a hologram for fine correction are also possible. They can use a single wave sensor such as a camera located in the hologram plane and serving as the holographic detector. Its signal can indeed provide a wavefront map to activate a deformable mirror in the entrance aperture. It can also be fed to a dynamic holographic plate, incorporating its own actuators, in the form of the fringe patterns acting as tiny gratings within each of its speckles. Like ordinary actuators in a servo loop, their performance is degraded by photon noise in the control signals, i.e. the recorded fringes with their "frozen" photon noise. During the observation, after the hologram recording stage, the more usual form of "live" photon noise is also present in the recorded image and further contributes to degrading the detectability of a planet's peak if its level is not much higher than the surrounding speckle peaks.

In our simulations, we have included both the "frozen" and the "live" photon noise contributions. We assumed that exposures of equal duration served for the two phases of hologram recording and observation. This may be optimal if the hologram is recorded with the same star which is subsequently observed. If, however, a brighter reference star or a laser artificial star serves to record the hologram, the results given below may be considered as a lower limit since the photon noise of the hologram becomes attenuated in this latter case. Poisson-distributed photon noise was generated in the hologram and the final image using a standard IDL routine, based on C code (Press et al. 1992).

Starting from the best solution, i.e. a hologram with an apodized reference beam and without a twin wave, we assumed 60 s exposures, both in recording the hologram and observing, using a 6.5 m aperture in the V band (550 nm), with a filter width of 10 nm. The results are shown in Figs. 8 and 9 (simulations at $\lambda/20$ and $\lambda/100$ respectively).

We see that the photon noise is negligible for stellar magnitudes brighter than 7 (at $\lambda/20$) and 3 (at $\lambda/100$); the hologram performance is then maximal, and independent from the

star magnitude. In our simulation, those magnitudes correspond to about $\approx 3 \times 10^6$ (at $\lambda/20$) and $\approx 3 \times 10^8$ (at $\lambda/100$) photons per speckle in the hologram, and their performances are degraded below this value.

Above magnitude 13 (at $\lambda/20$) and 11 (at $\lambda/100$), where the hologram has $\approx 3 \times 10^4$ (at $\lambda/20$) and $\approx 2 \times 10^5$ (at $\lambda/100$) photons per speckle, the sensitivity gain vanishes with respect to a Lyot apodized coronagraph without a hologram.

With a ground-based telescope, affected by "seeing", bright stars may provide enough photons during brief exposures, shorter than the lifetime of "seeing", to activate both a conventional adaptive optics system giving a high Strehl ratio, and, within the coronagraphic attachment, the recording of a dynamic hologram. On fainter stars, a bright Laser Guide Star may similarly serve for both stages of adaptive correction.

In space, where the wavefront bumpiness is greatly reduced and varies much more slowly, some planet detection sensitivity can be gained by recording the hologram on a star brighter than the star observed, or on a ground-based laser source (which is not affected by turbulence if its emitting aperture is unresolved).

It could be of interest if the hologram could attenuate the fixed stellar speckles escaping the adaptive correction. We attempted to address this by replacing ψ_d with a sum of a constant and a randomly variable term, in Eq. (2), but did not elucidate the matter. Further work with simulations will be useful.

6. Discussion

In the following subsections, two aspects for the future development of the instrument are considered: the chromatism of the coronagraph with a hologram; and the problems introduced by a star that is poorly resolved.

6.1. Achromatizing a hologram

The fringe spacing in the hologram is normally proportional to wavelength but can be made invariant if the deviating prism (see Fig. 1) in the reference beam is replaced by a diffraction grating. If the grating operates in the first order, its angular dispersion indeed increases the incidence angle of light at increasing wavelengths. This can reduce the hologram's wavelength sensitivity, both during the recording stage and the observations, and increase the usable spectral bandwidth, although the speckles contributed by the direct beam are also wavelength-dependant. Further simulations, achieved with a range of wavelengths, would be of interest to specify the bandwidth then achievable.

Another approach involves a Lippmann-Bragg hologram, i.e. a thick hologram where the fringes are patterned as stratifications throughout the depth of the recording layer. These can be wavelength-multiplexed, and can simultaneously reconstruct the variously colored wavefronts that have been recorded. Some recording materials, such as lithium niobate single crystals or polymeric compounds (Shishido & Ikeda 2007), are erasable and re-usable. Their moderate recording sensitivity however may require a bright laser star.

6.2. Resolved parent star

The original Lyot coronagraph is highly tolerant of a star being resolved, as demonstrated by its initial success on the solar corona. However, a star which is slightly resolved by the telescope or hypertelescope (Labeyrie 1996; Le Coroller et al. 2004) can degrade the hologram recorded with its light, and also degrade the nulling depth in the image cleaned by a pre-recorded hologram. In both cases, what matters is the invariance of the hologram, particularly in terms of fringe positions, with respect to a slight motion of a point star. Such motion produces identical translation shifts of the central and peripheral focal patterns separated by the micro-prism. The fringe pattern recorded in the hologram, located at a nearly infinite distance in the relayed pupil, is therefore nearly invariant. The pupil indeed remains fixed, and both interfering wavefronts reaching it become tilted by the same amount, while their phase difference is invariant. Their speckle detail is however slightly modified by the varying edge effects at the boundaries of the micro-prism and field lens. The hologram is thus expected to be somewhat tolerant of a resolved star serving to record it. Similarly, a hologram recorded on a point source and then used to observe a resolved star is also expected to efficiently null its coronagraphic residue, since the live fringes remain contrasted. Further simulations and laboratory experiments will be of interest to estimate the tolerable apparent size of the star vs. the desired nulling depth.

7. Conclusions

Our diffractive analysis and simulations of a holographic coronagraph, and the comparison with other forms of adaptive coronagraphy, show that the theoretical photon-limited sensitivity in detecting faint exo-planets is comparable. These methods will therefore need to be compared in terms of their technical implementations. Hybrid methods, for example combining an adaptive mirror before the occulter and a hologram after, are likely to be similarly limited by the photon noise but may also have practical merits, such as relaxing the accuracy of the actuators (Putnam et al. 2006).

Depending on the holographic processes and materials that will become available, various forms of practical implementation may be of interest. With some re-writable holograms using amplifying photo-sensitive materials, no electronic image processing may be needed. Instead, and for a better flexibility, the recording and diffractive functions may be separated, using respectively a camera and a spatial light modulator.

With $\lambda/20$ wavefront bumpiness, the planet detection limit is improved, in terms of star/planet flux ratio, from $10^{4.5}$ to $10^{7.9}$. In terms of photon noise, we found that the hologram improves the performance of the coronagraph if it is recorded with more than $\approx 3 \times 10^4$ photons per speckle. With $\lambda/100$ wavefront bumpiness, the detection limit improves from $10^{5.7}$ to $10^{10.8}$, and the hologram improves the performance of the coronagraph if it is recorded with more than $\approx 2 \times 10^5$ photons per speckle.

We also discussed ways of making this holographic technique achromatic, and its tolerance for a poorly resolved star. In order to reach the best results, a thick Lippmann-Bragg hologram is of interest to remove the twin wave, but it restricts the range of available holographic components. Following laboratory simulations, already initiated, tests on ground-based adaptive telescopes may be possible with available camera and Spatial Light Modulator components.

References

Aime, C., Soummer, R., & Ferrari, A. 2002, A&A, 389, 334

Chauvin, G., Lagrange, A.-M., Dumas, C., et al. 2004, A&A, 425, L29

Codona, J. L., & Angel, R. 2004, ApJ, 604, L117

Guyon, O. 2003, A&A, 404, 379

Guyon, O., Angel, R., Bowers, C., et al. 2007, in American Astronomical Society Meeting Abstracts, 210, 33.08

Kalas, P., Graham, J. R., Chiang, E., et al. 2008, ArXiv e-prints

Labeyrie, A. 1996, A&AS, 118, 517

Labeyrie, A. 2004, in EAS PS–12, ed. C. Aime, & R. Soummer, 3

Labeyrie, A., & Le Coroller, H. 2004, in New Frontiers in Stellar Interferometry, ed. W. A. Traub (Bellingham, WA: The International Society for Optical Engineering), Proc. SPIE, 5491, 90

Labeyrie, A., Lipson, S., & Nisenson, P. 2006, An Introduction to Astronomical Interferometry, ed. A. Labeyrie, S. Lipson, & P. Nisenson (Cambridge, UK: Cambridge University Press)

Le Coroller, H., Dejonghe, J., Arpesella, C., Vernet, D., & Labeyrie, A. 2004, A&A, 426, 721

Lyot, B. 1939, MNRAS, 99, 580

Marois, C., Macintosh, B., Barman, T., et al. 2008, ArXiv e-prints

Mawet, D., Riaud, P., Hanot, C., et al. 2007, in Proc. SPIE, 6693, 52

Mayor, M., Queloz, D., Marcy, G., et al. 1995, IAU Circ., 6251, 1

Perez, J. P. 2000, Optique: fondements et applications (Dunod Masson Sciences)

Press, W., Teukolsky, S., Vetterling, W., & Flannery, B. 1992, Numerical Recipes in C, 2nd edn. (Cambridge, UK: Cambridge University Press)

Putnam, N., Codona, J. L., & Angel, J. R. P. 2006, in SPIE Conf. Ser., 6272

Riaud, P., Boccaletti, A., Rouan, D., Lemarquis, F., & Labeyrie, A. 2001, PASP, 113, 1145

Riaud, P., Boccaletti, A., Baudrand, J., & Rouan, D. 2003, PASP, 115, 712

Roddier, F., & Roddier, C. 1997, PASP, 109, 815

Shishido, A., & Ikeda, T. 2007, in SPIE Conf. Ser., 6587

Soummer, R., Aime, C., & Falloon, P. E. 2003, A&A, 397, 1161

Soummer, R., Pueyo, L., Sivaramakrishnan, A., & Vanderbei, R. J. 2007, Optics Express, 15, 15935

Swain, M. R., Vasisht, G., Tinetti, G., et al. 2009, ApJ, 690, L114